

Article

Fabrication and Characterization of Plasma Sprayed TiO_2 and $\text{Li}_4\text{Ti}_5\text{O}_{12}$ Materials as All Active Material Lithium-Ion Battery Electrodes

Dean Yost¹, Jonathan Laurer², Kevin Childrey² , Chen Cai¹ and Gary M. Koenig, Jr^{1,*}

¹ Department of Chemical Engineering, University of Virginia, 102 Engineers Way, Charlottesville, VA 22904, USA; czt4dc@virginia.edu (D.Y.); cc2nj@virginia.edu (C.C.)

² Commonwealth Center for Advanced Manufacturing, 5520 West Quaker Road, Disputanta, VA 23842, USA; jonathan.laurer@ccam-va.com (J.L.); kevin.childrey@ccam-va.com (K.C.)

* Correspondence: gary.koenig@virginia.edu; Tel.: +1-(434)-982-2714; Fax: +1-(434)-982-2658

Abstract: Two strategies to increase battery energy density at the cell level are to increase electrode thickness and to reduce the amount of inactive electrode constituents. All active material (AAM) electrodes provide a route to achieve both of those aims toward high areal capacity electrodes. AAM electrodes are often fabricated using hydraulic compression processes followed by thermal treatment; however, additive manufacturing routes could provide opportunities for more time-efficient and geometry-flexible electrode fabrication. One possible route for additive manufacturing of AAM electrodes would be to employ plasma spray as a direct additive manufacturing technology, and AAM electrode fabrication using plasma spray will be the focus of the work herein. TiO_2 and $\text{Li}_4\text{Ti}_5\text{O}_{12}$ (LTO) powders were deposited onto stainless steel substrates via plasma spray processing to produce AAM battery electrodes, and evaluated with regards to material and electrochemical properties. The TiO_2 electrodes delivered low electrochemical capacity, $<12 \text{ mAh g}^{-1}$, which was attributed to limitations of the initial feed powder. LTO plasma sprayed AAM electrodes had much higher capacity and were comparable in total capacity at a low rate of discharge to composite electrodes fabricated using the same raw powder feed material. LTO material and electrochemical properties were sensitive to the plasma spray conditions, suggesting that tuning the material microstructure and electrochemical properties is possible by controlling the plasma spray deposition parameters.

Keywords: plasma spray; thick electrode; additive manufacturing; lithium ion battery



Citation: Yost, D.; Laurer, J.; Childrey, K.; Cai, C.; Koenig, G.M., Jr.

Fabrication and Characterization of Plasma Sprayed TiO_2 and $\text{Li}_4\text{Ti}_5\text{O}_{12}$ Materials as All Active Material Lithium-Ion Battery Electrodes.

Batteries **2023**, *9*, 598. <https://doi.org/10.3390/batteries9120598>

Academic Editors: Catia Arbizzani and Jae-won Lee

Received: 7 November 2023

Revised: 2 December 2023

Accepted: 13 December 2023

Published: 17 December 2023



Copyright: © 2023 by the authors. Licensee MDPI, Basel, Switzerland. This article is an open access article distributed under the terms and conditions of the Creative Commons Attribution (CC BY) license (<https://creativecommons.org/licenses/by/4.0/>).

1. Introduction

Electronic devices have found increasing integration into everyday life, which results in a corresponding increasing demand for power that drives their operation [1]. Revenues for wearable electronics are projected to increase from USD 80.5 billion to USD 255.6 billion from 2021 to 2026, and these devices continue to move toward sleeker designs and more advanced applications [2]. As battery-powered wearable electronics become even more prevalent, more reliable/extended power supply and custom device geometry may be drivers of consumer preference. Lithium (Li)-ion batteries are the modern standard for portable electronics energy storage with a long history of development dating back to at least 1958 [3]. A variety of different materials and systems have been investigated for further improvements and understanding of battery properties [4,5]. The most common materials used in Li-ion consumer electronics applications include LiCoO_2 (LCO) cathode active material paired with graphite anode active material, where both materials are processed into thin composite electrodes containing inactive conductive additives and binders. Researchers have pushed efforts to increase the energy density of these batteries through various methods from altering the electrochemical materials used to redesigning the electrode architecture [6–11].

Many material alternatives to graphite and LCO have been investigated depending on the battery application and use case [12]. TiO₂ materials have been investigated as an alternative anode material to graphite [13–15]. TiO₂ has a lower reported volume expansion with lithiation/delithiation (4–8%) compared to graphite (7–12%) and silicon (320%), which can mitigate electrode degradation during cycling [16–18]. An additional consideration is that the stable reversible gravimetric capacity of TiO₂ is lower than graphite (at ~200 mAh g⁻¹, although the theoretical capacity for reduction of each Ti⁴⁺ to Ti³⁺ would be ~336 mAh g⁻¹) [19–21]. The average voltage of TiO₂ is at ~1.5 V (vs. Li/Li⁺), which is also higher than graphite, resulting in a lower cell voltage when paired with a cathode but mitigating the likelihood of Li metal deposition because the potential is so much further from Li metal [21,22]. A titanium oxide material that has seen more maturity in Li-ion battery applications is Li₄Ti₅O₁₂ (LTO). LTO has a spinel phase crystal structure and is commonly referred to as a “zero-strain” material due to a <1% volume expansion during lithiation/delithiation cycling being desirable for extended cyclability (within the lithiated compositional window of up to Li₇Ti₅O₁₂) [23]. LTO has an average intercalation potential for Li⁺ slightly lower than TiO₂, and LTO also has a very flat potential for intercalation/deintercalation at 1.55 V (vs. Li/Li⁺) [24].

In addition to changing the material chemistry, the modification of electrode geometry and microstructure can be used to control and improve electrochemical cell properties [25,26]. Commercial Li-ion electrodes are composites containing electroactive material that participates in electrochemical reactions and inactive additives. The inactive components are polymer binders that improve mechanical properties and impart flexibility to the electrodes and conductive additives (e.g., carbon black), which provide high matrix electronic conductivity [27]. Commercial composite electrodes contain roughly 5–10 wt.% conductive additives and 2 wt.% polymer binder [28–31]. Despite the necessity of the inactive content in composite electrodes, they occupy weight and volume within the electrode microstructure without contributing to deliverable energy. These additives also restrict ion transport within the microstructure and increase interfacial overpotentials, resulting in relative increases in cell polarization which, at a minimum, reduces charge/discharge energy efficiency and will also restrict rate capability depending on the limiting processes within the cell [32]. By modifying the composition or structure of these composite electrodes the aforementioned drawbacks can be mitigated.

Processing limitations of composite electrodes are a consideration concerning the resulting electrode geometry and microstructure. The electroactive material, polymer binder, and conductive additive are combined with a solvent to form a slurry, which is cast onto the current collector. To ensure a homogeneous distribution of components in the dried slurry, the casting thickness must generally be restricted to prevent the settling of denser components. Finding process alternatives to increase electrode thickness has captured research attention because thicker electrodes require fewer auxiliary components for assembly to achieve the same active material amount. Auxiliary components that do not participate in the chemical reaction include current collectors, porous membrane separators, and wiring. For example, increasing composite electrode thickness from 25 μm to 200 μm was estimated to decrease the auxiliary weight ratio from 44% to 12% [33]. Alternative techniques have been developed by researchers to avoid the previously mentioned issues associated with producing homogenous thick electrodes.

Sintering has proven feasible for processing thick electrodes, achieving thicknesses >200 μm and minimizing or eliminating binders and conductive additives [34]. One route to fabricate such electrodes involves coating active material with polymer binder and hydraulically pressing it into a pellet, which is subsequently thermally treated to achieve mild sintering and binder burn-out. The resulting porous electrode pellet is comprised of entirely active material, denoting these electrodes as all-active material (AAM) electrodes. Additional manufacturing methods for AAM electrodes include 3D printing, freeze-drying, selective etching, and other templating methods [35,36]. These electrodes are different relative to conventional composites in that they achieve greater thicknesses and eliminate

non-electroactive additives contained within the electrode. AAM electrodes also have been demonstrated for multiple material constituents, meaning that advances in materials chemistry may be able to be combined with energy density improvements due to electrode microstructure and processing.

In this work, plasma spray deposition was investigated as a method to directly deposit thick AAM electrodes for Li-ion batteries. Plasma spray can be used as an additive manufacturing process that adheres a feed material as a thin film via deposition onto a target substrate. Plasma spray processing has potential advantages as a manufacturing technique for producing battery electrodes due to its ability to be applied onto curved and complex substrates, generating relatively uniform coating layers across wide substrate areas, and having good adhesion between the sprayed material thin film and the target substrate. These are important characteristics especially for additive and/or custom battery electrode geometry systems where electrode stability, formability, and current collector adhesion can be a challenge. Feed powder is melted in a high-energy plasma jet and then deposited via splattering. One of the materials evaluated in this work, TiO_2 , has a history of use as dense plasma sprayed coatings for abrasion/heat resistance. A potential challenge in using plasma spray for battery electrodes is that typically plasma sprayed coatings are targeted to have low porosities, for example in the range of 5–15% [37]. In comparison, AAM electrodes are often in the range of 30–40 vol% porosity, which is filled with electrolyte during cell fabrication, and this porosity is necessary to mitigate ion transport limitations within thick AAM electrodes [9]. Using plasma spray to directly fabricate battery electrodes has not had many reports, although there have been reports using plasma spray to synthesize battery active material powder. As an example, Chang et al. successfully synthesized LTO particles by plasma spraying a precursor containing lithium and titanium, but that powder was subsequently processed and evaluated in a conventional composite electrode [38]. Other recent reports have investigated both LCO and LTO materials experiencing plasma spray conditions during processing [39–41]. Relatively thick AAM plasma sprayed electrodes are expected to provide further opportunity as a case with a unique electrode architecture utilizing plasma spray. Herein, TiO_2 and LTO powder were directly plasma sprayed onto a current collector for use as an AAM electrode within a battery cell. Potential advantages of using plasma spray to fabricate AAM electrode cells include reducing the number of intermediate steps in battery assembly by directly adhering the active material to the cell casing, and enabling deposition onto more complex geometries that are inaccessible using prior AAM electrode fabrication methods.

2. Materials and Methods

2.1. Plasma Spray Electrode Fabrication

Plasma spraying was conducted at the Commonwealth Center for Advanced Manufacturing (CCAM). Plasma spray coatings were applied using a Praxair TFA SG-100 plasma gun with powders delivered by a rotary powder hopper. The two oxide powders deposited using plasma spray were TiO_2 (Oerlikon Metco (New York, NY, USA), AMDRY) and $\text{Li}_4\text{Ti}_5\text{O}_{12}$ (LTO, Nanomyte[®] BE-10, NEI Corporation, Somerset, NJ, USA). For both oxide powders, polyester powder (Metco 600NS, 60–90 μm) was co-injected to increase the porosity of the deposited films. After coating, any residual polyester domains were removed by heating the coated substrates at 500 °C for 3 h in air. The final porosities for the oxide films were 30–40% on a volume basis.

The plasma was rastered across the substrate surface using a 6-axis ABB IRB-2600 industrial robot (Zurich, Switzerland), in a ladder pattern defined by conditions in Table 1. Plasma conditions for each deposition can be found in Table 2. In the case of LTO, two power conditions were explored denoted as “high intensity” and “low intensity”. For all depositions, the targets/substrates were 2 cm^2 discs of 304 stainless steel with a thickness of 0.61 mm. The steel substrates were prepped by grit blasting with aluminum oxide grit in an Empire PF-4848 grit blast cabinet (Langhorne, PA, USA). After blasting, the resulting

surface roughness averaged 2.4 μm as determined using a Mitutoyo SJ-210 profilometer (Kawasaki, Japan).

Table 1. Raster path conditions used during plasma spray processing.

| Parameter | LTO | TiO ₂ |
|-------------------------------------|------|------------------|
| Standoff Distance [mm] | 120 | 150 |
| Surface Speed [mm s ⁻¹] | 1250 | 1250 |
| Step Size [mm] | 3 | 3 |

Table 2. Detailed plasma spray process conditions for the three electrodes evaluated in this work.

| Parameter | TiO ₂ | LTO (High Intensity) | LTO (Low Intensity) |
|-------------------------------------------------------------------------------------|------------------|----------------------|---------------------|
| Jambox Voltage [V] | 70 | 78 | 55 |
| Gun Current [A] | 330 | 230 | 200 |
| Gun Powder [kW] | 23 | 18 | 11 |
| Argon Flow (Primary) [$\times 10^{-3}$ m ³ s ⁻¹] | 0.783 | 1.50 | 1.33 |
| Hydrogen Flow (secondary) [$\times 10^{-3}$ m ³ s ⁻¹] | 0.200 | 0.200 | 0.030 |
| Powder Feed Rate [g min ⁻¹] | 20 | 15 | 15 |
| Polyester Feed Rate [g min ⁻¹] | 5 | 4 | 12 |

Plasma sprayed TiO₂ or LTO on steel substrates, after polyester burn out, were used directly as electrodes in battery cells.

2.2. Material Characterization

Material structural analysis was conducted using powder X-ray diffraction (XRD, PANalytical X'pert ProMPD, Almelo, The Netherlands). Scanning electron microscope (SEM, Quanta 650 FEG-SEM, Hillsboro, OR, USA) images were obtained on received powders, and for powders after processing, using plasma spray or hydraulic compression and heating.

2.3. AAM Electrode Fabrication

AAM electrodes (that were not plasma spray deposited) were prepared to have a similar composition and thickness to the plasma sprayed electrodes. The LCO active material used for electrode fabrication was custom synthesized, with the procedures adapted from co-precipitation and calcination methods previously reported [42]. AAM electrodes were prepared by blending active material powder (LCO, TiO₂, LTO) with 2 wt.% polyvinyl butyral (PVB, Pfals & Bauer, Waterbury, CT, USA) binder in ethanol, with a ratio of 2 mL PVB solution per 1.0 g active material. The slurry was mixed via mortar and pestle until all ethanol solvent evaporated. The PVB-coated powder was spread in a 16 mm diameter Carver pellet die and pressed at 5.3×10^4 N for 2 min using a Carver 4350 manual bench top press to fabricate porous pellets. Pellets were fired under an air atmosphere at 600 °C for 2 h with ramping rates for heating and cooling of 1 °C/minute in a Carbolite CWF 1300 box furnace. AAM electrodes were adhered to a stainless-steel disc using a conductive paste. The paste was made using a 1:1 by weight polyvinylpyrrolidone (Sigma Aldrich, St. Louis, MO, USA): Super P carbon black (Alfa Aesar, Ward Hill, MA, USA) slurry with ethanol solvent. After the adhesion of the AAM electrode to the stainless steel, the ethanol was evaporated under vacuum at 80 °C for a minimum of 30 min in a VWR vacuum oven. For AAM electrodes, the loading was 174, 144, and 140 mg cm⁻² for LCO, TiO₂, and LTO, respectively. Based on dimensions and reported true density for the electroactive materials, the porosity for LCO, TiO₂, and LTO AAM electrodes was 0.32, 0.40, and 0.41.

Composite electrodes were fabricated using an 80:10:10 active material:polymer binder:conductive carbon ratio. For composite electrodes made with TiO₂ active material, the powder was first fired to 600 °C in an air atmosphere before being processed into an electrode because for the other processes (either plasma spray or AAM thermal processing) the powder was exposed to elevated temperatures. A 12 wt.% Poly(vinylidene fluoride) binder (PVDF, Alfa Aesar) solution dissolved in N-2-Methyl-2-Pyrrolidone (NMP) solvent was used as the slurry base. Active material and conductive carbon were dispersed in the binder solution with equal amounts of NMP solvent to active material added in a conditioning mixer (Thinky AR-100, Tokyo, Japan). The slurry was blended for 3 min mixing and 3 min defoaming to achieve the desired consistency. The resulting slurries were deposited onto an aluminum foil sheet via a doctor blade with a 250 µm gap before drying overnight at 70 °C. Dried composites were punched into 1.6 cm² discs and assembly of these electrodes into battery cells occurred in an argon glovebox. Composite electrode loading was 6.3 mg cm⁻². Stainless steel 2032 coin cell components were used with a microporous separator (Celgard 2325, Charlotte, NC, USA) immersed in 0.1 mL of electrolyte (1.2 M LiPF₆ in 3:7 ethyl methyl carbonate, BASF, Ludwigshafen, Germany) to assemble the cell.

2.4. Electrochemical Characterization

Plasma sprayed electrodes were paired with either a Li metal anode (100 µm thickness foil, Livent, Philadelphia, PA, USA) or an AAM LCO cathode. For AAM LCO electrodes, the pellet mass was targeted to achieve a 1.35:1 capacity ratio relative to the plasma sprayed LTO anode, where assumed gravimetric capacities for cell balancing were 175 mAh g⁻¹ LTO and 135 mAh g⁻¹ LCO.

Electrochemical characterization for AAM or plasma sprayed LTO or TiO₂ electrodes was evaluated using either lithium metal anode half cells or LCO cathode full cells. All cells were assembled in an argon atmosphere glovebox with two layers of Celgard 2325 microporous separators punched to size (~16 mm diameter circles), and 0.2 mL of electrolyte (1.2 M LiPF₆ in 3:7 ethylene carbonate:ethyl methyl carbonate, BASF). Half cells were constructed with an AAM cathode paired with two layers of lithium metal as an anode. TiO₂ cells were discharged to a lower voltage cutoff of 0.5 V (vs. Li/Li⁺) at a C rate of C/5000 (assuming a 200 mAh g⁻¹ TiO₂ basis, resulting in a current density of 3.3 µA cm⁻²). LTO plasma sprayed cells were discharged to a lower voltage cutoff of 1.0 V (vs. Li/Li⁺) at C/1000 (assuming a 175 mAh g⁻¹ LTO basis, corresponding to a current density of 20.7 µA cm⁻²). An AAM LTO cell was discharged using the same lower voltage cutoff of 1.0 V at C/100. AAM LTO electrodes have shown high gravimetric capacity utilization relative to the theoretical benchmark as thick AAM electrodes in prior reports [43], allowing more aggressive cycling conditions (higher C rate) with the LTO electrode cells. For full cells with LTO anodes (AAM or plasma sprayed) and LCO cathodes (AAM), the voltage window during cycling was 1.0 to 3.0 V (cell).

Electrochemical impedance spectroscopy (EIS, Gamry Reference 600) was conducted using both AAM and plasma sprayed TiO₂ electrodes. The TiO₂ was the working electrode/cathode and Li metal was used as both the counter and reference electrode (anode). The coin cells were fabricated using the same methods described above. EIS was conducted both on freshly prepared cells and after the discharge procedure concluded. The EIS was performed with an amplitude of ±10 mV over a frequency range of 1 × 10⁵ Hz to 0.1 Hz.

3. Results

3.1. TiO₂ Electrodes

In choosing a material to implement as a plasma sprayed battery electrode, there are tradeoffs with regards to the availability of materials with properties desirable for plasma spray deposition and materials with desirable electrochemical properties (particularly when being fabricated into an AAM architecture). TiO₂ is a material readily available with powders targeted for spray deposition applications, though in many cases the target is dense coatings for protection of the underlying substrate [44,45]. Prior reports depositing

TiO₂ via cold plasma spray in temperatures ranging from 200–1000 °C have demonstrated the deposited films' ability to obtain targeted crystal structures, morphologies, and particle size [46–48]. Our initial plasma spray electrode system used TiO₂ because of the availability of commercial plasma spray powders of this material, as well as the extensive literature on the use of TiO₂ as a Li-ion battery anode material. The commercial TiO₂ powder used had dense particles with sharp edges and sizes typically ranging from 38–70 μm (Figure 1A), where the size and density of the particles would be desirable from a plasma spray deposition application standpoint. Achieving uniform flow characteristics in the plasma jet can be more challenging for finer particles, thus powders for spray applications often have particle sizes between 10–100 μm, with medians around 40 μm [49,50]. From an electrochemical standpoint, large particles will generally result in less interfacial surface area for reaction compared to smaller particles and have larger solid-state ionic and electronic transport distances at the particle level. Both of these outcomes can negatively impact the utilization of available electrochemical capacity for electrodes comprised of these particles, particularly at increasing rates of charge/discharge [51].

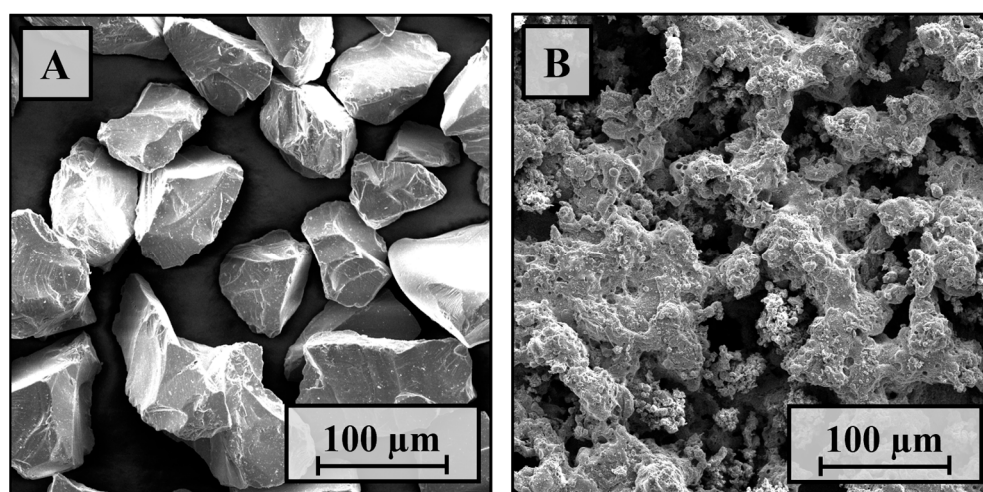


Figure 1. SEM images of (A) received TiO₂ powder prior to plasma spray and (B) plasma sprayed TiO₂ electrode.

An additional component included during the plasma spray deposition was polyester powder, which was co-injected with the TiO₂ powder. The polyester was co-injected to increase the deposited film porosity, and any residual polyester was burned out via a thermal post-treatment on the deposited film and substrate. The concern was that if the films were too dense, the ion transport through the microstructure would be too restricted to achieve capacity at reasonable current densities. For relatively thick electrodes, ion transport through the microstructure, in many cases, is the greatest source of cell overpotential and charge/discharge polarization [52]. Electrodes must have sufficient porosity to allow the electrolyte to percolate through the electrode, facilitating interfacial reactions between the solid–solvent interface. In forming the resulting plasma sprayed TiO₂ electrodes (Figure 1B) the particles completely melted and created an interlocking web of active material upon impacting the substrate. The average thickness of the TiO₂ electrodes was 523 μm, and with the polyester burned-off, processing was successful at making a thick porous AAM electrode. Due to the particles melting and depositing, additional surface area was exposed to the electrolyte for electrochemical reactions.

TiO₂ has multiple crystalline phases, with rutile and anatase being the most common polymorphs, that can appear under different processing conditions. The anatase phase has been reported previously for the reversible electrochemical insertion/deinsertion of Li⁺ [53]. Rutile is the most thermodynamically stable phase, and TiO₂ has been reported to convert to rutile after elevated temperature processing [54]. XRD was used to assess the impact plasma spray processing had on the TiO₂ phase. The purchased TiO₂ had a

blend of different phases, although many of the peaks were consistent with the rutile TiO_2 phase (Figure 2). After plasma spraying the TiO_2 , all XRD peaks were consistent with the rutile phase material. The purchased TiO_2 powder was only used after thermal treatment, and after heating, the impurity phases were no longer apparent in XRD, and patterns were consistent with only the rutile phase being present. Peaks from the reference rutile sample were consistent with the pattern produced with the samples after plasma spray (JPCS 88-1175) [55].

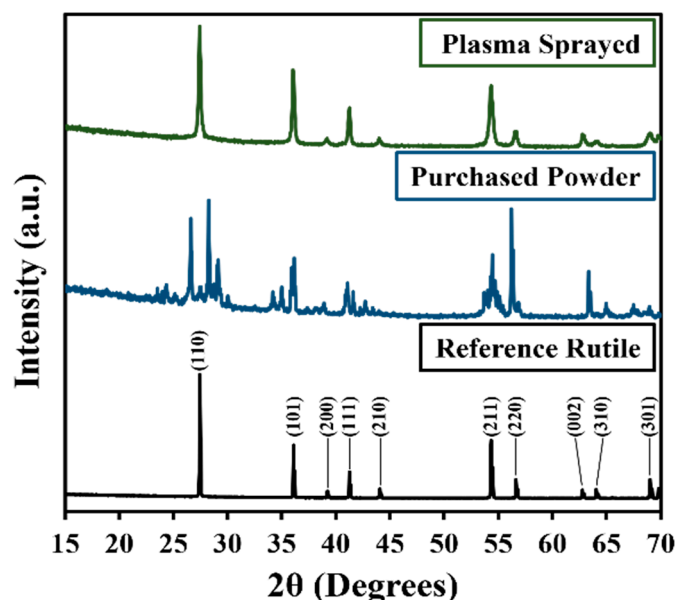


Figure 2. X-ray diffraction patterns for purchased TiO_2 powder (blue, middle) and the resulting thin film after plasma spraying (green, top). Bottom pattern shows reference for rutile phase TiO_2 (JPCS 88-1175).

For the electrochemical evaluation of the plasma sprayed TiO_2 electrodes, coin cells were fabricated with Li metal anodes and discharged at extremely slow rates ($C/5000$, which corresponded to $2.6 \mu\text{A cm}^2$). Electrodes were discharged at such slow rates, where achieving full assumed theoretical capacity would take 5000 h, to mitigate cell polarization. With TiO_2 reducing from Ti^{4+} to Ti^{3+} in the voltage range between 1.4–1.8 V (vs. Li/Li^+), the electrodes were discharged down to 0.5 V (vs. Li/Li^+) to access capacity even if there was still high polarization in the cell [56]. Discharge of the cells provided significantly less capacity than anticipated, with much of the capacity being delivered well below the lower expected range of the potential of 1.4 V (vs. Li/Li^+) (Figure 3). At 0.5 V (vs. Li/Li^+), the plasma sprayed TiO_2 electrode only provided roughly 5 mAh g^{-1} , compared to the 200 mAh g^{-1} prior reported reversible capacity for other TiO_2 materials [19]. Despite the low operating voltage and capacity, the voltage profiles suggested some lithium insertion into rutile TiO_2 [21]. These results indicated the electrode had high resistance due to either the intrinsic properties of the purchased material and/or a consequence of the plasma spray processing.

Hydraulically pressed and mildly sintered AAM electrodes were fabricated using the same purchased TiO_2 powder, as detailed in Section 2, for comparison to plasma sprayed counterparts. The two electrodes (AAM and plasma sprayed) had similar compositions and thicknesses, and thus the electrochemical characteristics were expected to be similar. The electrode thickness and porosity were targeted to values similar to prior thick AAM electrode reports [42,57]. XRD of the AAM indicated the thermal treatment during processing was sufficient to similarly convert the purchased TiO_2 to a rutile phase (XRD pattern can be found in Supplementary Materials, Figure S1). Discharging to the same cutoff voltage and using the same targeted C rate, the AAM electrode provided slightly more capacity

(11 mAh g⁻¹ at 0.5 V (vs. Li/Li⁺)) than the plasma sprayed electrode. As AAM processing has previously resulted in reversible cycling of Li-ion active materials with high capacity utilization [58], the low capacity from both AAM and plasma sprayed electrodes was not expected to result from the manufacturing processes but was attributed to the intrinsic properties of the purchased TiO₂ material.

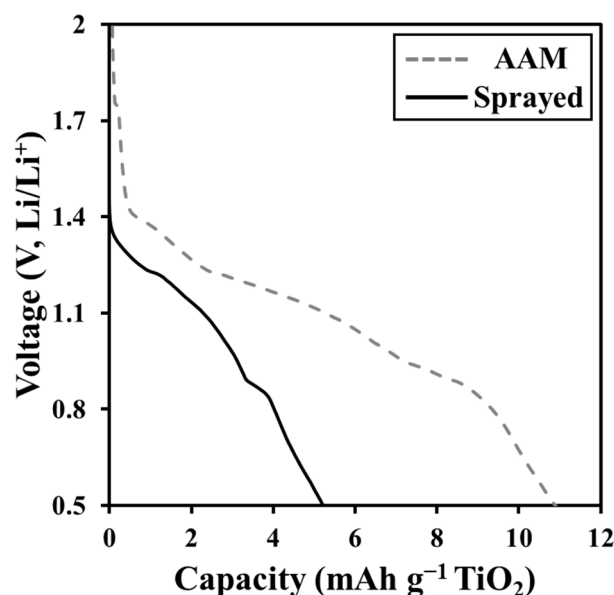


Figure 3. Constant current discharge profiles of all active material (dashed line) and plasma sprayed (solid line) electrodes of TiO₂ at C/5000. Anode was Li metal.

Both the plasma sprayed and AAM TiO₂ electrodes had very low capacity relative to previous reports for TiO₂ Li-ion electrodes [19–21], though the AAM electrode had slightly higher capacity. Improved electrolyte access to the pores in the AAM electrode may have resulted in higher capacity, although, as noted, both electrodes were still well below other reports for TiO₂ materials. Many of the prior TiO₂ reports used composite electrodes, and thus the original TiO₂ feed powder was heat treated under the same conditions as the AAM electrodes to convert to the rutile phase (XRD of the heated powder can be found in Supplementary Materials, Figure S1) and then processed into a composite electrode. Composite electrodes are generally much thinner than the plasma sprayed or AAM electrodes and conductive carbon additives should provide high electrode matrix electronic conductivity. Thus, the composite would be expected to overcome the ionic and electronic transport limitations that would be shared for the plasma sprayed and AAM electrodes. However, the composite TiO₂ electrodes also provided a low capacity of <25 mAh g⁻¹ when discharged down to 0.5 V (vs. Li/Li⁺) (discharge profile can be found in Supplementary Materials, Figure S2). This result suggested the intrinsic electrochemical capacity (e.g., mAh g⁻¹ TiO₂) of the particles themselves was relatively low compared to other TiO₂ Li-ion electrode reports [59]. The root cause of this low capacity was not exhaustively investigated; however, it is noted that due to the targeted use in plasma spray applications, the particles were much larger than typical battery electrode particles. Their size would result in both relatively high interfacial overpotential due to limited electrochemically active area and overpotential due to relatively large solid state Li⁺ transport distances to access the interior of the particles during lithiation [60]. Smaller particles have been previously explored as an approach to reduce solid-state diffusion resistance and increase surface area for faradaic reactions to provide capacity [61,62]. Preliminary EIS was conducted for insights into sources of TiO₂ resistance as both AAM and plasma sprayed electrodes, where the EIS was performed both after initially fabricating the cell (paired with Li metal counter/reference electrode) and after the discharge process. The

resulting Nyquist plots can be found in Supplementary Materials, Figure S3. A summary of extracted equivalent circuit parameters from the EIS can also be found in Supplementary Materials, Table S1. The initial high-frequency intercept value was higher for the AAM electrode cell compared to the plasma sprayed cell. Because all other cell components were the same besides the TiO_2 , it was speculated that this difference resulted from lower resistance for the contact point(s) between the TiO_2 and current collector for the plasma sprayed sample. The high-frequency intercept resistance also increased dramatically after discharge for the AAM electrode, which may have been due to mechanical damage after the lithiation of an even more resistive TiO_2 -current collector contact. Based on other reports, it was expected that the resistance associated with the semicircle region (associated with charge transfer and interfacial processes) would decrease with lithiation [63,64]. However, the opposite trend was observed where both cells had this resistance increase after discharge. We again speculate that volumetric expansion and mechanical damage of the electrodes may have resulted in this trend, but detailed analysis of this hypothesis will be left to future investigations. Despite the low TiO_2 capacity after plasma spraying, there was still some electrochemical capacity, which was at an appropriate voltage range that indicated Ti reduction within the oxide. Thus, we explored using a titanium oxide-based material that was explicitly produced for Li-ion anode applications and investigated if the material could be deposited as a robust and electrochemically active electrode via plasma spray processing.

3.2. $\text{Li}_4\text{Ti}_5\text{O}_{12}$ Electrodes

LTO was evaluated next as a plasma sprayed Li-ion electrode using commercially purchased LTO powder. This material has been characterized in multiple reports as an AAM electrode where high capacity, comparable to that from the same source material processed into thinner composite electrodes, can be achieved [65–68]. LTO also has minimal volume change during lithiation/delithiation, which would be expected to aid in maintaining the mechanical integrity of the plasma sprayed film during charge/discharge cycling [69]. An additional consideration for LTO is that with the intense thermal energy from plasma spray, the crystal structure/composition of LTO could change. For example, Li may be lost from the material structure, and/or a combination of new Li-rich and Li-poor titanium oxide phases may result. Thus, it was expected that with LTO there may be a tradeoff between higher intensity/temperature plasma processing, which would likely result in better adhesion between the fed LTO material and the substrate, and lower intensity/temperature plasma, which would favor maintaining the LTO structure and composition.

LTO particles were significantly smaller than the TiO_2 raw material discussed earlier. The LTO primary particles were often less than 1 μm and formed larger porous aggregates (Figure 4A), compared to the 38–70 μm TiO_2 particles. LTO material was selected due to prior stable electrochemical cycling in AAM electrodes, rather than for expected flow properties into the plasma jet. While running the risk of powder flow limitations, the smaller particles provided potential benefits of increased gravimetric surface area. Two conditions were used to produce plasma sprayed LTO electrodes, corresponding to a “high intensity” and “low intensity” plasma jet. The high-intensity conditions were nominally the same as those used for the plasma sprayed TiO_2 electrodes. Low-intensity conditions were implemented to mitigate thermal impacts on the LTO structure while being sufficient to successfully deposit and adhere material onto the substrate. SEM imaging showing individual splats can be seen for both intensity spray parameters (Figure 4B,C). High-intensity LTO had a similar electrode morphology as the TiO_2 electrode, with less branched connections. Low-intensity LTO had more defined splats relative to the high-intensity LTO due to the lower thermal heating of the particles when exposed to the plasma jet under low-intensity spray conditions. These results indicated even the low-intensity parameters still achieved the necessary energy to melt and deposit LTO splats onto the target substrate surface.

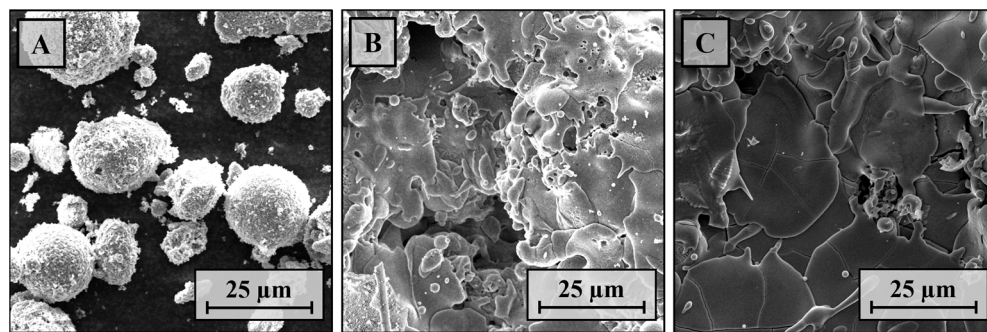


Figure 4. SEM images of (A) LTO particles before processing, (B) LTO after high-intensity plasma spray, and (C) LTO after low-intensity plasma spray.

The impact of plasma spray processing on LTO crystal structure was evaluated with XRD (Figure 5). The rutile reference pattern was the same as that used previously for TiO_2 [55]. The LTO powder as purchased was used for the LTO reference pattern and aligned well with accepted literature for its structure (JCPDS 26-1198) [70,71]. Both high and low-intensity plasma sprayed films had a blend of peaks consistent with both $\text{Li}_4\text{Ti}_5\text{O}_{12}$ and rutile TiO_2 phases. Comparatively, the high-intensity film had higher relative intensity peaks consistent with rutile phase (110) and (211) planes compared to the low-intensity plasma sprayed material. The low-intensity plasma sprayed film had a much higher relative intensity peak consistent with the (400) peak for LTO. The trend of having comparatively more lithium-lean phases in the high-intensity plasma film was consistent with the loss of Li from the LTO phase under the thermal stress within the plasma jet. The unassigned peaks at 20° , 22° , and 25° would potentially support this Li loss from the LTO material. Both the 20° and 22° peaks, marked by † symbols, were speculated to result from the beta- Li_2TiO_3 phase being present in the film (JCPDS 33-0831) [72,73]. The presence of this Li-rich impurity would balance the net stoichiometry from the formation of the Li-lean rutile phase, though it is possible there was some net total Li loss in the material. The peak at 25° , marked by ✱, was speculated to be contributed by the anatase phase TiO_2 (101) peak (JCPDS 84-1286) and had greater intensity in the high-intensity condition where more Li would be expected to be lost from the LTO material [55]. Overall, the XRD results suggested that the plasma sprayed LTO resulted in blended phases, mostly comprised of LTO and rutile TiO_2 , where the relative presence of the phases was determined by the intensity of the plasma jet. By further optimizing the plasma jet parameters to decrease jet intensity (while maintaining good substrate adherence), it is expected it should be possible to further decrease the relative ratio of the rutile TiO_2 phase.

The plasma sprayed LTO electrodes were evaluated electrochemically as primary cells (only had a single discharge) in a similar manner to the sprayed TiO_2 electrodes. Electrodes were paired with Li metal anodes and lithiated at a low current. For the plasma sprayed LTO, the electrodes were expected to have less polarization than the TiO_2 and were thus discharged at C/1000, which was still a very slow rate but facilitated completing the discharge in a more reasonable total time. Electrochemically, in the literature, LTO has been reported with a plateau voltage of 1.55 V (vs. Li/Li^+) and a reversible capacity of 175 mAh g^{-1} between a 1.0–2.5 V (vs. Li/Li^+) operating window [74,75]. In contrast with the TiO_2 samples, the LTO cells were not discharged below 1.0 V to avoid over-lithiation, which can occur for LTO between 0.5–1.0 V (vs. Li/Li^+) [76]. Both high and low-intensity plasma sprayed LTO electrodes achieved significantly more capacity than the TiO_2 electrodes while displaying characteristic LTO discharge plateau regions (Figure 6A). Consistent with the higher fraction of LTO phase observed in XRD patterns, the low-intensity electrode had a longer (higher capacity) plateau, which was indicative of having more of the $\text{Li}_4\text{Ti}_5\text{O}_{12}$ phase present for the electrochemical reaction than high-intensity electrode. After the voltage dropped at the end of the plateau region associated with LTO, the discharge profile for both sprayed electrodes had an elbow at 1.42 V (vs. Li/Li^+).

The additional capacity was speculated to have been provided by the electrochemical capacity of one of the other Ti oxide phases present in the materials, such as rutile or anatase TiO₂ because of the XRD patterns (Figure 5) suggesting the presence of these minority phases and the voltage profile associated with the capacity [21]. The high-intensity plasma sprayed electrode had higher capacity in the shoulder region, again consistent with higher relative fractions of other titanium oxide phases for the higher-intensity electrode as observed in XRD. Overall, the low-intensity LTO electrode provided an amount of capacity, 169 mAh g⁻¹, closer to the intrinsic capacity of the LTO material.

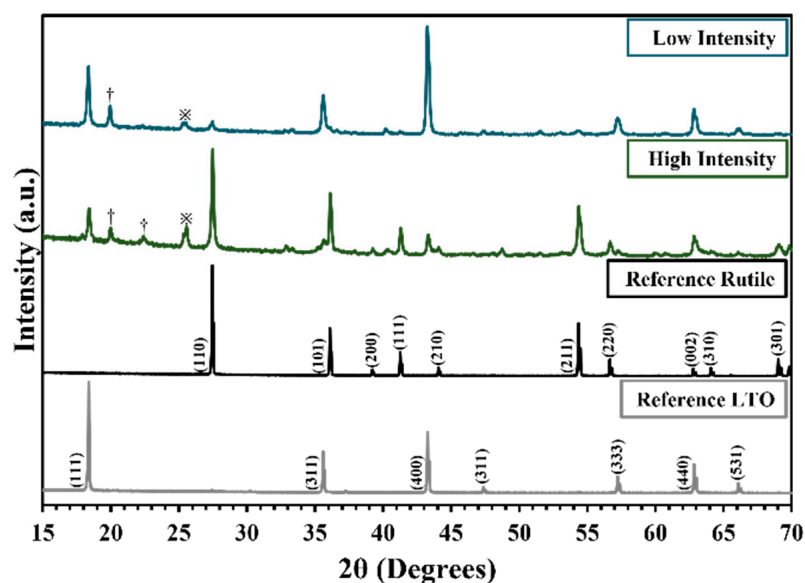


Figure 5. XRD patterns of plasma sprayed LTO at low (blue) and high (green) plasma jet intensities. Li₄Ti₅O₁₂ (JCPDS 26-1198) and rutile phase TiO₂ (JCPDS 88-1175) are provided for reference. † indicates peaks consistent with beta-Li₂TiO₃ (JCPDS 33-0831) and * indicates peaks consistent with anatase phase TiO₂ (JCPDS 84-1286).

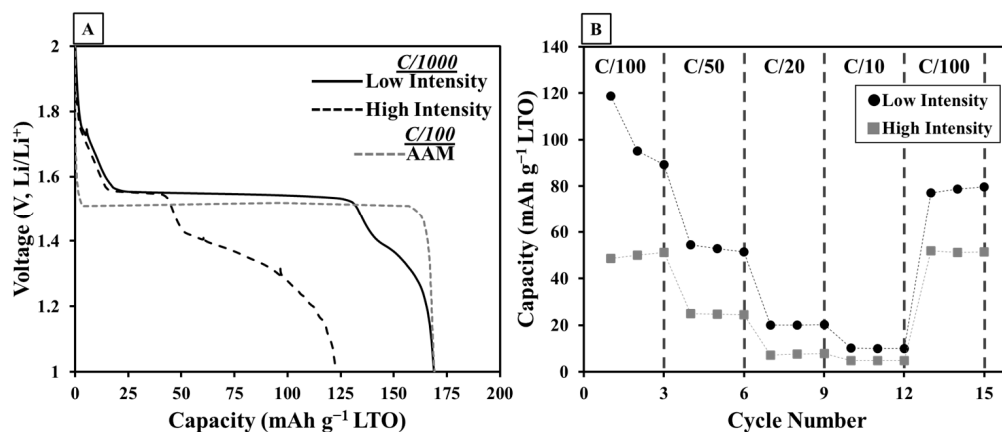


Figure 6. (A) Constant current discharge curves as primary cells for plasma sprayed LTO electrodes with low (solid black) and high (black dashed) plasma jet intensities. All active material LTO electrode (gray dashed) is provided for comparison. Each electrode was paired with a Li metal anode. (B) Discharge capacity for plasma sprayed LTO electrodes fabricated using low (black circles) and high (grey squares) intensity plasma jet settings. Cathodes were AAM LCO electrodes and the voltage window was 1.0 to 3.0 V (cell). For reference, C/100 corresponded to 0.18 mA cm⁻².

Although the plasma sprayed electrodes delivered significant electrochemical capacity and provided proof-of-concept for spray-deposited LTO battery electrodes, AAM LTO electrodes were also fabricated to provide comparative discharge profiles for the same material using similar thick electrode architectures and compositions but without as dramatic of morphology or structural changes as occurs with plasma processing. As previous studies of AAM LTO electrodes have demonstrated higher rate capability, C/100 was still expected to be a sufficiently low current to not encounter major polarization limitations on delivered capacity. The AAM LTO electrode had a nearly identical delivered capacity as the low-intensity plasma sprayed electrode. The high electrochemical capacity for the LTO AAM electrodes further supported that the TiO₂ used for plasma sprayed electrodes had intrinsic material limitations that limited electrochemical outcomes and were not limited by the plasma spray processing of the material. Regardless, using too high of a plasma gun intensity leads to a change in the LTO material crystalline phase and can result in material degradation and loss of electrochemical capacity. With electrochemical properties dependent on the plasma spray parameters, the low-intensity jet revealed that adjusting the spraying conditions provided robust and high-capacity electrodes. Optimizing plasma jet parameters provides a potential avenue for further improvement of plasma sprayed electrodes.

Given that the plasma-sprayed LTO electrodes achieved relatively high capacity and that LTO AAM electrodes have previously been cycled through charge/discharge for many reversible cycles, multiple charge/discharge cycles for plasma sprayed LTO were evaluated in a full cell. These LTO electrodes were thick, thus charge/discharge cycling paired with Li metal was not explored as with the high areal capacity (>18 mAh cm⁻²) cycling limitations as the reactivity of the Li metal with the electrolyte would make assessment of the LTO electrode reversibility challenging [77,78]. Thus, the plasma sprayed LTO electrodes were used as anodes and paired with LCO AAM cathodes. The LCO cathodes were not plasma sprayed and were produced with the AAM fabrication method mentioned in Section 2. LCO was selected as it has been previously used as a high areal capacity AAM electrode paired with AAM LTO in multiple reports [42,79,80]. The AAM LCO electrodes were designed to have a slight excess of capacity relative to the LTO based on the LTO active material mass (in other words, the cells were LTO limited based on an assumption of 175 mAh g⁻¹ LTO). Rate capability evaluation of LTO/LCO full cells where LTO was plasma sprayed and the LCO was an AAM electrode can be found in Figure 6B (representative charge/discharge profiles at different rates can be found in Supplementary Materials, Figure S4). High- and low-intensity sprayed electrodes were examined within the voltage window 1.0–3.0 V (cell) from C/100 to C/10 (where C/10 corresponded to 1.8 mA cm⁻²). Relatively low current densities were applied for the LTO/LCO full cells compared to traditional rate capability tests due to the relatively large electrode thicknesses. As a result, the rate capability outcomes were intended to inform electrode capacity retention at increasing charge rates. More capacity was provided by the low-intensity plasma sprayed LTO than the high-intensity sprayed LTO at all discharge rates, and both electrodes still provided >40 mAh g⁻¹ by the end of the rate capability evaluation. LTO was expected to have an improved cyclability in relation to other titanium oxides due to low volume change and high electronic conductivity after slight lithiation [81].

The low-intensity LTO electrode experienced more capacity fade with cycling when comparing the first and last cycles at C/100 relative to the high-intensity LTO electrode. The low-intensity electrode did achieve higher discharge capacity for all cycles, despite the greater relative loss of capacity. It is possible, though speculative, that the lower intensity LTO electrode may have had less robust adhesion to the current collector, which impacted the electrode/current collector interface and thus retention of capacity and access to the electrode active material with cycling. Future studies on the tradeoffs in material, mechanical, and electrochemical properties as a function of plasma spray processing conditions will need to be pursued to better understand how these processing-property relationships evolve. The investigation of plasma electrodes was carried out with a relatively thick

electrode architecture, which inherently influenced the electrochemical properties due to mass transport limitations. The thickness of plasma sprayed electrodes can generally be controlled through the number of raster sweeps during plasma spray processing. The plasma sprayed electrodes were contrasted with hydraulically pressed and sintered AAM electrodes to provide insights into the influence of the plasma spray process environment on material and electrochemical properties. This report provides an initial evaluation of plasma sprayed LTO and TiO₂ electrodes and suggests that high-capacity LTO electrodes can be processed using this manufacturing method.

4. Conclusions

Plasma spraying was demonstrated as an approach to generate thick AAM electrode architectures directly deposited onto a current collector surface. Material selection for such applications must consider both the suitability to plasma spray processing and retention of material and electrochemical properties when exposed to the high-temperature plasma conditions during spraying. TiO₂ used in this study was well-suited to plasma spray processing, but the initial powder itself had intrinsic limitations to electrochemical cycling. Both plasma sprayed and AAM TiO₂ electrodes had very low electrochemical capacity even at a slow (C/5000) rate, with a capacity <10% the values reported for similar composition and phase materials in the literature. LTO was successfully deposited using plasma spray processing and provided electrodes with electrochemical capacity that approached the limits for this material. A plasma sprayed LTO electrode with lower-intensity plasma processing had a gravimetric capacity that approached the expected limit for LTO and was approximately the same as the capacity observed for an AAM LTO electrode. LTO also had material and electrochemical properties that were dependent on the plasma spray processing parameters, where with higher intensity processing there was evidence of higher relative amounts of impurity phases lean in Li composition that formed in the material. Understanding the interactions between plasma spray conditions and material properties will be important for future research into plasma spray battery electrodes. For example, producing plasma sprayed electrodes of varying thicknesses would provide insight into the thickness limits of plasma sprayed electrodes and how plasma sprayed microstructure influences electrochemical properties.

Supplementary Materials: The following supporting information can be downloaded at: <https://www.mdpi.com/article/10.3390/batteries9120598/s1>, Figure S1: X-ray diffraction patterns of purchased TiO₂ powder; Figure S2: Discharge profile of heat treated purchased TiO₂ powder; Figure S3: Nyquist plots from EIS of TiO₂ AAM and plasma sprayed electrodes; Table S1: TiO₂ electrode resistances based off fitted Thevenin model; Figure S4: Charge/discharge voltage profiles of LTO/LCO AAM thick electrode full cells. Reference [82] is cited in the supplementary materials.

Author Contributions: Conceptualization, G.M.K.J. and J.L.; methodology, G.M.K.J. and J.L.; formal analysis, D.Y. and G.M.K.J.; investigation, D.Y., C.C., G.M.K.J. and J.L.; resources, K.C.; data curation, D.Y.; writing—original draft preparation, D.Y.; writing—review and editing, D.Y., G.M.K.J. and J.L.; project administration, K.C.; funding acquisition, G.M.K.J. and K.C. All authors have read and agreed to the published version of the manuscript.

Funding: This research was supported by seed funding from the Commonwealth Center for Advanced Manufacturing.

Data Availability Statement: The data presented in this study are available on request from the corresponding author. The data are not publicly available due to privacy.

Conflicts of Interest: The authors declare no conflict of interest. The funders had no role in the design of the study; in the collection, analyses, or interpretation of data; in the writing of the manuscript; or in the decision to publish the results.

References

1. Koenig, G.M.; Liu, N. Lithium-Ion Batteries and Their Impact on Our Lives. *Electrochem. Soc. Interface* **2022**, *31*, 55. [[CrossRef](#)]

2. Sumboja, A.; Liu, J.; Zheng, W.G.; Zong, Y.; Zhang, H.; Liu, Z. Electrochemical Energy Storage Devices for Wearable Technology: A Rationale for Materials Selection and Cell Design. *Chem. Soc. Rev.* **2018**, *47*, 5919–5945. [[CrossRef](#)] [[PubMed](#)]
3. Reddy, M.V.; Mauger, A.; Julien, C.M.; Paolella, A.; Zaghbi, K. Brief History of Early Lithium-Battery Development. *Materials* **2020**, *13*, 1884. [[CrossRef](#)] [[PubMed](#)]
4. Deng, W.N.; Li, Y.H.; Xu, D.F.; Zhou, W.; Xiang, K.X.; Chen, H. Three-Dimensional Hierarchically Porous Nitrogen-Doped Carbon from Water Hyacinth as Selenium Host for High-Performance Lithium–Selenium Batteries. *Rare Met.* **2022**, *41*, 3432–3445. [[CrossRef](#)]
5. Wen, X.; Luo, J.; Xiang, K.; Zhou, W.; Zhang, C.; Chen, H. High-Performance Monoclinic WO₃ Nanospheres with the Novel NH₄⁺ Diffusion Behaviors for Aqueous Ammonium-Ion Batteries. *Chem. Eng. J.* **2023**, *458*, 141381. [[CrossRef](#)]
6. Andre, D.; Kim, S.J.; Lamp, P.; Lux, S.F.; Maglia, F.; Paschos, O.; Stiaszny, B. Future Generations of Cathode Materials: An Automotive Industry Perspective. *J. Mater. Chem. A Mater.* **2015**, *3*, 6709–6732. [[CrossRef](#)]
7. Qi, Z.; Koenig, G.M. Review Article: Flow Battery Systems with Solid Electroactive Materials. *J. Vac. Sci. Technol. B Nanotechnol. Microelectron. Mater. Process. Meas. Phenom.* **2017**, *35*, 040801. [[CrossRef](#)]
8. Lai, W.; Erdonmez, C.K.; Marinis, T.F.; Bjune, C.K.; Dudney, N.J.; Xu, F.; Wartena, R.; Chiang, Y.M. Ultrahigh-Energy-Density Microbatteries Enabled by New Electrode Architecture and Micropackaging Design. *Adv. Mater.* **2010**, *22*, E139–E144. [[CrossRef](#)]
9. Huang, C.; Dontigny, M.; Zaghbi, K.; Grant, P.S. Low-Tortuosity and Graded Lithium Ion Battery Cathodes by Ice Templating. *J. Mater. Chem. A Mater.* **2019**, *7*, 21421–21431. [[CrossRef](#)]
10. Li, L.; Erb, R.M.; Wang, J.; Wang, J.; Chiang, Y.M. Fabrication of Low-Tortuosity Ultrahigh-Area-Capacity Battery Electrodes through Magnetic Alignment of Emulsion-Based Slurries. *Adv. Energy Mater.* **2019**, *9*, 1802472. [[CrossRef](#)]
11. Wu, J.; Ju, Z.; Zhang, X.; Quilty, C.; Takeuchi, K.J.; Bock, D.C.; Marschilok, A.C.; Takeuchi, E.S.; Yu, G. Ultrahigh-Capacity and Scalable Architected Battery Electrodes via Tortuosity Modulation. *ACS Nano* **2021**, *15*, 19109–19118. [[CrossRef](#)] [[PubMed](#)]
12. Nitta, N.; Wu, F.; Lee, J.T.; Yushin, G. Li-Ion Battery Materials: Present and Future. *Mater. Today* **2015**, *18*, 252–264. [[CrossRef](#)]
13. Djenizian, T.; Hanzu, I.; Knauth, P. Nanostructured Negative Electrodes Based on Titania for Li-Ion Microbatteries. *J. Mater. Chem.* **2011**, *21*, 9925–9937. [[CrossRef](#)]
14. Zhang, Y.; Jiang, Z.; Huang, J.; Lim, L.Y.; Li, W.; Deng, J.; Gong, D.; Tang, Y.; Lai, Y.; Chen, Z. Titanate and Titania Nanostructured Materials for Environmental and Energy Applications: A Review. *RSC Adv.* **2015**, *5*, 79479–79510. [[CrossRef](#)]
15. Liang, S.; Wang, X.; Cheng, Y.J.; Xia, Y.; Müller-Buschbaum, P. Anatase Titanium Dioxide as Rechargeable Ion Battery Electrode—A Chronological Review. *Energy Storage Mater.* **2022**, *45*, 201–264. [[CrossRef](#)]
16. Koudriachova, M.V.; Harrison, N.M.; de Leeuw, S.W. Density-Functional Simulations of Lithium Intercalation in Rutile. *Phys. Rev. B Condens. Matter Mater. Phys.* **2002**, *65*, 2354231. [[CrossRef](#)]
17. Willenberg, L.K.; Dechent, P.; Fuchs, G.; Sauer, D.U.; Figgemeier, E. High-Precision Monitoring of Volume Change of Commercial Lithium-Ion Batteries by Using Strain Gauges. *Sustainability* **2020**, *12*, 557. [[CrossRef](#)]
18. Parekh, M.H.; Sediako, A.D.; Naseri, A.; Thomson, M.J.; Pol, V.G. In Situ Mechanistic Elucidation of Superior Si-C-Graphite Li-Ion Battery Anode Formation with Thermal Safety Aspects. *Adv. Energy Mater.* **2020**, *10*, 1902799. [[CrossRef](#)]
19. Madian, M.; Eychemüller, A.; Giebel, L. Current Advances in TiO₂-Based Nanostructure Electrodes for High Performance Lithium Ion Batteries. *Batteries* **2018**, *4*, 7. [[CrossRef](#)]
20. Xu, Y.; Zhou, M.; Wen, L.; Wang, C.; Zhao, H.; Mi, Y.; Liang, L.; Fu, Q.; Wu, M.; Lei, Y. Highly Ordered Three-Dimensional Ni-TiO₂ Nanoarrays as Sodium Ion Battery Anodes. *Chem. Mater.* **2015**, *27*, 4274–4280. [[CrossRef](#)]
21. Dambournet, D.; Belharouak, I.; Amine, K. Tailored Preparation Methods of TiO₂ Anatase, Rutile, Brookite: Mechanism of Formation and Electrochemical Properties. *Chem. Mater.* **2010**, *22*, 1173–1179. [[CrossRef](#)]
22. Ortiz, G.F.; Hanzu, I.; Djenizian, T.; Lavela, P.; Tirado, J.L.; Knauth, P. Alternative Li-Ion Battery Electrode Based on Self-Organized Titania Nanotubes. *Chem. Mater.* **2009**, *21*, 63–67. [[CrossRef](#)]
23. Mukai, K.; Kato, Y.; Nakano, H. Understanding the Zero-Strain Lithium Insertion Scheme of Li[Li_{1/3}Ti_{5/3}]O₄: Structural Changes at Atomic Scale Clarified by Raman Spectroscopy. *J. Phys. Chem. C* **2014**, *118*, 2992–2999. [[CrossRef](#)]
24. Pohjalainen, E.; Rauhala, T.; Valkeapää, M.; Kallioinen, J.; Kallio, T. Effect of Li₄Ti₅O₁₂ Particle Size on the Performance of Lithium Ion Battery Electrodes at High C-Rates and Low Temperatures. *J. Phys. Chem. C* **2015**, *119*, 2277–2283. [[CrossRef](#)]
25. Miranda, D.; Almeida, A.M.; Lanceros-Méndez, S.; Costa, C.M. Effect of the Active Material Type and Battery Geometry on the Thermal Behavior of Lithium-Ion Batteries. *Energy* **2019**, *185*, 1250–1262. [[CrossRef](#)]
26. Song, J.; Bazant, M.Z. Effects of Nanoparticle Geometry and Size Distribution on Diffusion Impedance of Battery Electrodes. *J. Electrochem. Soc.* **2013**, *160*, A15–A24. [[CrossRef](#)]
27. Mayer, J.K.; Almar, L.; Asylbekov, E.; Haselrieder, W.; Kwade, A.; Weber, A.; Nirschl, H. Influence of the Carbon Black Dispersing Process on the Microstructure and Performance of Li-Ion Battery Cathodes. *Energy Technol.* **2020**, *8*, 1900161. [[CrossRef](#)]
28. Jouhara, A.; Dupré, N.; Guyomard, D.; Lakraychi, A.E.; Dolhem, F.; Poizot, P. Playing with the P-Doping Mechanism to Lower the Carbon Loading in n-Type Insertion Organic Electrodes: First Feasibility Study with Binder-Free Composite Electrodes. *J. Electrochem. Soc.* **2020**, *167*, 070540. [[CrossRef](#)]
29. Palomares, V.; Goñi, A.; De Muro, I.G.; De Meazza, I.; Bengoechea, M.; Cantero, I.; Rojo, T. Conductive Additive Content Balance in Li-Ion Battery Cathodes: Commercial Carbon Blacks vs. in Situ Carbon from LiFePO₄/C Composites. *J. Power Sources* **2010**, *195*, 7661–7668. [[CrossRef](#)]

30. Gaikwad, A.M.; Arias, A.C. Understanding the Effects of Electrode Formulation on the Mechanical Strength of Composite Electrodes for Flexible Batteries. *ACS Appl. Mater. Interfaces* **2017**, *9*, 6390–6400. [[CrossRef](#)]
31. Ligneel, E.; Lestriez, B.; Guyomard, D. Relationships between Processing, Morphology and Discharge Capacity of the Composite Electrode. *J. Power Sources* **2007**, *174*, 716–719. [[CrossRef](#)]
32. Foreman, E.; Zakri, W.; Hossein Sanatimoghaddam, M.; Modjtahedi, A.; Pathak, S.; Kashkooli, A.G.; Garafolo, N.G.; Farhad, S. A Review of Inactive Materials and Components of Flexible Lithium-Ion Batteries. *Adv. Sustain. Syst.* **2017**, *1*, 1700061. [[CrossRef](#)]
33. Kuang, Y.; Chen, C.; Kirsch, D.; Hu, L. Thick Electrode Batteries: Principles, Opportunities, and Challenges. *Adv. Energy Mater.* **2019**, *9*, 1901457. [[CrossRef](#)]
34. Singh, M.; Kaiser, J.; Hahn, H. Thick Electrodes for High Energy Lithium Ion Batteries. *J. Electrochem. Soc.* **2015**, *162*, A1196–A1201. [[CrossRef](#)]
35. Wang, F.; Lee, J.; Chen, L.; Zhang, G.; He, S.; Han, J.; Ahn, J.; Cheong, J.Y.; Jiang, S.; Kim, I.D. Inspired by Wood: Thick Electrodes for Supercapacitors. *ACS Nano* **2023**, *17*, 8866–8898. [[CrossRef](#)]
36. Elango, R.; Demortière, A.; De Andrade, V.; Morcrette, M.; Seznec, V. Thick Binder-Free Electrodes for Li-Ion Battery Fabricated Using Templating Approach and Spark Plasma Sintering Reveals High Areal Capacity. *Adv. Energy Mater.* **2018**, *8*, 1703031. [[CrossRef](#)]
37. Curry, N.; Leitner, M.; Körner, K. High-Porosity Thermal Barrier Coatings from High-Power Plasma Spray Equipment—Processing, Performance and Economics. *Coatings* **2020**, *10*, 957. [[CrossRef](#)]
38. Chang, S.M.; Rodríguez Tolava, E.F.; Yang, Y.J.; Li, H.C.; Lee, R.C.; Wu, N.L.; Hsu, C.C. One-Step Fast Synthesis of Li₄Ti₅O₁₂ Particles Using an Atmospheric Pressure Plasma Jet. *J. Am. Ceram. Soc.* **2014**, *97*, 708–712. [[CrossRef](#)]
39. Hsueh, T.-H.; Tsai, C.-H.; Liu, S.-E.; Wang, M.-C.; Chang, S.-M.; Shiue, A.; Chin, K.-Y. LiCoO₂ Battery Electrode Fabricated by High Deposition-Rate Atmospheric Plasma Spraying for Lithium Battery. *J. Electrochem. Soc.* **2022**, *169*, 100506. [[CrossRef](#)]
40. Wu, X.; Liang, X.; Zhang, X.; Lan, L.; Li, S.; Gai, Q. Structural Evolution of Plasma Sprayed Amorphous Li₄Ti₅O₁₂ Electrode and Ceramic/Polymer Composite Electrolyte during Electrochemical Cycle of Quasi-Solid-State Lithium Battery. *J. Adv. Ceram.* **2021**, *10*, 347–354. [[CrossRef](#)]
41. Liang, X.; Wang, Y.; Zhang, X.; Han, D.; Lan, L.; Zhang, Y. Performance Study of a Li₄Ti₅O₁₂ Electrode for Lithium Batteries Prepared by Atmospheric Plasma Spraying. *Ceram. Int.* **2019**, *45*, 23750–23755. [[CrossRef](#)]
42. Robinson, J.P.; Ruppert, J.J.; Dong, H.; Koenig, G.M. Sintered Electrode Full Cells for High Energy Density Lithium-Ion Batteries. *J. Appl. Electrochem.* **2018**, *48*, 1297–1304. [[CrossRef](#)]
43. Zhang, H.; Yang, Y.; Xu, H.; Wang, L.; Lu, X.; He, X. Li₄Ti₅O₁₂ Spinel Anode: Fundamentals and Advances in Rechargeable Batteries. *InfoMat* **2022**, *4*, e12228. [[CrossRef](#)]
44. Gardon, M.; Guilemany, J.M. Milestones in Functional Titanium Dioxide Thermal Spray Coatings: A Review. *J. Therm. Spray Technol.* **2014**, *23*, 577–595. [[CrossRef](#)]
45. Chen, D.; Jordan, E.H.; Gell, M.; Ma, X. Dense TiO₂ Coating Using the Solution Precursor Plasma Spray Process. *Proc. J. Am. Ceram. Soc.* **2008**, *91*, 865–872. [[CrossRef](#)]
46. Yang, G.J.; Li, C.J.; Han, F.; Li, W.Y.; Ohmori, A. Low Temperature Deposition and Characterization of TiO₂ Photocatalytic Film through Cold Spray. *Appl. Surf. Sci.* **2008**, *254*, 3979–3982. [[CrossRef](#)]
47. Herrmann-Geppert, I.; Bogdanoff, P.; Emmler, T.; Dittrich, T.; Radnik, J.; Klassen, T.; Gutzmann, H.; Schieda, M. Cold Gas Spraying—A Promising Technique for Photoelectrodes: The Example TiO₂. *Catal. Today* **2016**, *260*, 140–147. [[CrossRef](#)]
48. Winnicki, M.; Baszczuk, A.; Jasiorski, M.; Borak, B.; Małachowska, A. Preliminary Studies of TiO₂ Nanopowder Deposition onto Metallic Substrate by Low Pressure Cold Spraying. *Surf. Coat. Technol.* **2019**, *371*, 194–202. [[CrossRef](#)]
49. Stanford, M.K.; DellaCorte, C.; Eylon, D. Particle Size Effects on Flow Properties of PS304 Plasma Spray Feedstock Powder Blend. In *27th Annual Cocoa Beach Conference on Advanced Ceramics and Composites: A: Ceramic Engineering and Science Proceedings*; Ceramic Engineering and Science Proceeding (CESP); American Ceramic Society: Westerville, OH, USA, 2003; Volume 24, pp. 577–586.
50. Vardelle, A.; Moreau, C.; Themelis, N.J.; Chazelas, C. A Perspective on Plasma Spray Technology. *Plasma Chem. Plasma Process.* **2015**, *35*, 491–509. [[CrossRef](#)]
51. Shin, J.Y.; Samuelis, D.; Maier, J. Sustained Lithium-Storage Performance of Hierarchical, Nanoporous Anatase TiO₂ at High Rates: Emphasis on Interfacial Storage Phenomena. *Adv. Funct. Mater.* **2011**, *21*, 3464–3472. [[CrossRef](#)]
52. Vu, A.; Qian, Y.; Stein, A. Porous Electrode Materials for Lithium-Ion Batteries—How to Prepare Them and What Makes Them Special. *Adv. Energy Mater.* **2012**, *2*, 1056–1085. [[CrossRef](#)]
53. Zlámalová, M.; Pitřna Lásková, B.; Vinarčíková, M.; Zukalová, M.; Kavan, L. Inherent Electrochemical Activity of TiO₂ (Anatase, Rutile) Enhances the Charge Capacity of Cathodes of Lithium-Sulfur Batteries. *J. Solid State Electrochem.* **2022**, *26*, 639–647. [[CrossRef](#)]
54. Smith, S.J.; Stevens, R.; Liu, S.; Li, G.; Navrotsky, A.; Boerio-Goates, J.; Woodfield, B.F. Heat Capacities and Thermodynamic Functions of TiO₂ Anatase and Rutile: Analysis of Phase Stability. *Am. Mineral.* **2009**, *94*, 236–243. [[CrossRef](#)]
55. Thamaphat, K.; Limsuwan, P.; Ngotawornchai, B. Phase Characterization of TiO₂ Powder by XRD and TEM. *Agric. Nat. Resour.* **2008**, *42*, 357–361.

56. Kubiak, P.; Fröschl, T.; Hüsing, N.; Hörmann, U.; Kaiser, U.; Schiller, R.; Weiss, C.K.; Landfester, K.; Wohlfahrt-Mehrens, M. TiO₂ Anatase Nanoparticle Networks: Synthesis, Structure, and Electrochemical Performance. *Small* **2011**, *7*, 1690–1696. [[CrossRef](#)]
57. Nie, Z.; Parai, R.; Cai, C.; Michaelis, C.; LaManna, J.M.; Hussey, D.S.; Jacobson, D.L.; Ghosh, D.; Koenig, G.M. Pore Microstructure Impacts on Lithium Ion Transport and Rate Capability of Thick Sintered Electrodes. *J. Electrochem. Soc.* **2021**, *168*, 060550. [[CrossRef](#)]
58. Cai, C.; Nie, Z.; Koenig, G.M. Multicomponent Two-Layered Cathode for Thick Sintered Lithium-Ion Batteries. *Mater. Adv.* **2022**, *3*, 4200–4212. [[CrossRef](#)]
59. Fischer, M.G.; Hua, X.; Wilts, B.D.; Gunkel, I.; Bennett, T.M.; Steiner, U. Mesoporous Titania Microspheres with Highly Tunable Pores as an Anode Material for Lithium Ion Batteries. *ACS Appl. Mater. Interfaces* **2017**, *9*, 22388–22397. [[CrossRef](#)]
60. Cai, C.; Hensley, D.; Koenig, G.M. Simulated Discharge Overpotential Distributions for Sintered Electrode Batteries in Rechargeable Coin Cell Form Factors. *J. Energy Storage* **2022**, *54*, 105218. [[CrossRef](#)]
61. Wagemaker, M.; Borghols, W.J.H.; Van Eck, E.R.H.; Kentgens, A.P.M.; Kearley, G.J.; Mulder, F.M. The Influence of Size on Phase Morphology and Li-Ion Mobility in Nanosized Lithiated Anatase TiO₂. *Chem. Eur. J.* **2007**, *13*, 2023–2028. [[CrossRef](#)]
62. Bakri, A.S.; Sahdan, M.Z.; Adriyanto, F.; Raship, N.A.; Said, N.D.M.; Abdullah, S.A.; Rahim, M.S. Effect of Annealing Temperature of Titanium Dioxide Thin Films on Structural and Electrical Properties. In *AIP Conference Proceedings*; American Institute of Physics Inc.: College Park, MD, USA, 2017; Volume 1788.
63. Deng, W.; Liu, W.; Zhu, H.; Chen, L.; Liao, H.; Chen, H. Click-Chemistry and Ionic Cross-Linking Induced Double Cross-Linking Ionogel Electrolyte for Flexible Lithium-Ion Batteries. *J. Energy Storage* **2023**, *72*, 108509. [[CrossRef](#)]
64. Moon, E.J.; Hong, J.K.; Mohanty, S.K.; Yang, M.; Ihm, K.; Lee, H.; Yoo, H.D. Coating Lithium Titanate Anodes with a Mixed Ionic-Electronic Conductor for High-Rate Lithium-Ion Batteries. *J. Power Sources* **2023**, *559*, 232657. [[CrossRef](#)]
65. Cai, C.; Yost, D.; Koenig, G.M. Increased Cycling Rates for Thick All Active Material Electrodes via Electrolyte Modifications. *J. Energy Storage* **2023**, *64*, 107238. [[CrossRef](#)]
66. Cai, C.; Koenig, G.M. Enhancing Low Electronic Conductivity Materials in All Active Material Electrodes through Multicomponent Architecture. *Energy Adv.* **2023**, *2*, 308–320. [[CrossRef](#)]
67. Sotomayor, M.E.; Torre-Gamarra, C.; de la Levenfeld, B.; Sanchez, J.Y.; Varez, A.; Kim, G.T.; Varzi, A.; Passerini, S. Ultra-Thick Battery Electrodes for High Gravimetric and Volumetric Energy Density Li-Ion Batteries. *J. Power Sources* **2019**, *437*, 226923. [[CrossRef](#)]
68. Deng, W.; Shi, W.; Liu, Q.; Jiang, J.; Li, X.; Feng, X. Constructing Gradient Porous Structure in Thick Li₄Ti₅O₁₂ Electrode for High-Energy and Stable Lithium-Ion Batteries. *ACS Sustain. Chem. Eng.* **2020**, *8*, 17062–17068. [[CrossRef](#)]
69. Parai, R.; Nie, Z.; Ghosh, D.; Koenig, G.M. Microstructure and Mechanical Properties of Electrochemically Cycled Ice-Templated Li₄Ti₅O₁₂ Sintered Anodes. *Int. J. Energy Res.* **2022**, *46*, 11501–11509. [[CrossRef](#)]
70. Lin, Y.S.; Duh, J.G. Facile Synthesis of Mesoporous Lithium Titanate Spheres for High Rate Lithium-Ion Batteries. *J. Power Sources* **2011**, *196*, 10698–10703. [[CrossRef](#)]
71. Lin, J.Y.; Hsu, C.C.; Ho, H.P.; Wu, S.H. Sol-Gel Synthesis of Aluminum Doped Lithium Titanate Anode Material for Lithium Ion Batteries. *Electrochim. Acta* **2013**, *87*, 126–132. [[CrossRef](#)]
72. Narayana, L.; Hussain, O.M.; Mauger, A.; Julien, C.M. Transport Properties of Nanostructured Li₂TiO₃ Anode Material Synthesized by Hydrothermal Method. *Science* **2019**, *1*, 39. [[CrossRef](#)]
73. Marthi, R.; Asgar, H.; Gadikota, G.; Smith, Y.R. On the Structure and Lithium Adsorption Mechanism of Layered H₂TiO₃. *ACS Appl. Mater. Interfaces* **2021**, *13*, 8361–8369. [[CrossRef](#)] [[PubMed](#)]
74. Cheng, C.; Liu, H.; Xue, X.; Cao, S.; Cao, H.; Shi, L. Synthesizing Nano-Sized (~20 Nm) Li₄Ti₅O₁₂ at Low Temperature for a High-Rate Performance Lithium Ion Battery Anode. *RSC Adv.* **2014**, *4*, 63105–63109. [[CrossRef](#)]
75. Ge, H.; Li, N.; Li, D.; Dai, C.; Wang, D. Study on the Theoretical Capacity of Spinel Lithium Titanate Induced by Low-Potential Intercalation. *J. Phys. Chem. C* **2009**, *113*, 6324–6326. [[CrossRef](#)]
76. Lu, X.; Gu, L.; Hu, Y.S.; Chiu, H.C.; Li, H.; Demopoulos, G.P.; Chen, L. New Insight into the Atomic-Scale Bulk and Surface Structure Evolution of Li₄Ti₅O₁₂ Anode. *J. Am. Chem. Soc.* **2015**, *137*, 1581–1586. [[CrossRef](#)] [[PubMed](#)]
77. Wu, B.; Lochala, J.; Taverne, T.; Xiao, J. The Interplay between Solid Electrolyte Interface (SEI) and Dendritic Lithium Growth. *Nano Energy* **2017**, *40*, 34–41. [[CrossRef](#)]
78. Wang, H.; Matsui, M.; Kuwata, H.; Sonoki, H.; Matsuda, Y.; Shang, X.; Takeda, Y.; Yamamoto, O.; Imanishi, N. A Reversible Dendrite-Free High-Areal-Capacity Lithium Metal Electrode. *Nat. Commun.* **2017**, *8*, 15106. [[CrossRef](#)]
79. Nie, Z.; Ong, S.; Hussey, D.S.; Lamanna, J.M.; Jacobson, D.L.; Koenig, G.M. Probing Transport Limitations in Thick Sintered Battery Electrodes with Neutron Imaging. *Mol. Syst. Des. Eng.* **2020**, *5*, 245–256. [[CrossRef](#)]
80. Nie, Z.; Parai, R.; Cai, C.; Ghosh, D.; Koenig, G.M. Improving High Rate Cycling Limitations of Thick Sintered Battery Electrodes by Mitigating Molecular Transport Limitations through Modifying Electrode Microstructure and Electrolyte Conductivity. *Mol. Syst. Des. Eng.* **2021**, *6*, 708–712. [[CrossRef](#)]

81. Young, D.; Ransil, A.; Amin, R.; Li, Z.; Chiang, Y.M. Electronic Conductivity in the $\text{Li}_4/3\text{Ti}_5/3\text{O}_4$ - $\text{Li}_7/3\text{Ti}_5/3\text{O}_4$ System and Variation with State-of-Charge as a Li Battery Anode. *Adv. Energy Mater.* **2013**, *3*, 1125–1129. [[CrossRef](#)]
82. Nikolian, A.; Fleurbaey, K.; Timmermans, J.-M.; De Hoog, J.; Fleurbaey, K.; Noshin, O.; Van De Bossche, P.; Van Mierlo, J. Classification of electric modeling and characterization methods of lithium-ion batteries for vehicle applications. In Proceedings of the European Electric Vehicle Congress 2014, Brussels, Belgium, 2–5 December 2014.

Disclaimer/Publisher's Note: The statements, opinions and data contained in all publications are solely those of the individual author(s) and contributor(s) and not of MDPI and/or the editor(s). MDPI and/or the editor(s) disclaim responsibility for any injury to people or property resulting from any ideas, methods, instructions or products referred to in the content.